



A new drone-borne GPR for soil moisture mapping

Kaijun Wu^{*}, Gabriela Arambulo Rodriguez, Marjana Zajc, Elodie Jacquemin, Michiels Clément, Albéric De Coster, Sébastien Lambot^{**}

Université catholique de Louvain, Earth and Life Institute, Croix du Sud 2, Box L7.05.02, 1348, Louvain-la-Neuve, Belgium

ARTICLE INFO

Keywords:

Ground-penetrating radar
GPR
Drone
Full-wave inversion
Soil moisture mapping

ABSTRACT

In this study, we set up a new drone-borne ground-penetrating radar (GPR) for soil moisture mapping. The whole radar system weighs 1.5 kg and consists of a handheld vector network analyzer (VNA) working as frequency domain radar, a lightweight hybrid horn-dipole antenna covering a wide frequency range (250–2800 MHz), a GPS for positioning, a microcomputer with the controlling application, and a smartphone for remote control. Soil moisture is derived from the radar data using full-wave inverse modeling based on the radar equation of Lambot et al. and multilayered media Green's functions. The inversion is performed in the time domain and focuses on the surface reflection. The antenna-drone system is characterized by global reflection and transmission functions which are determined through a calibration procedure. We performed drone-GPR measurements over three different agricultural fields in the loess belt region of Belgium. In this study, we used the 500–700 MHz range to avoid soil surface roughness effects and to focus on the top 10–20 cm of the soil. These fields present a range of landform conditions leading to specific soil moisture distributions. The soil moisture maps were constructed from the local measurements using kriging. The obtained soil moisture maps are in good agreement with the topographical conditions of the fields and aerial orthophotography observations. These results demonstrated the potential and benefits of drone-GPR for fast, high-resolution mapping of soil moisture at the field scale, and to support, e.g., precision agriculture and environmental monitoring.

1. Introduction

Water is supporting the survival of all organisms on the planet, and for humans, livestock and plants, the demanding for fresh water is increasing with the global population and economies growing. World agriculture consumes approximately 70% of the fresh water per year, 1970 l of water on average is used per person per day for all purposes like drinking, cooking, washing, etc. (Pimentel et al., 2004). Only about 2.5% of water on the earth is fresh water, 30% of which being stored as groundwater (Oki and Kanae, 2006). Although groundwater is generally regarded as a renewable resource in some cases because solar energy could transfer a great portion of water from oceans to lands by rainfall, its depletion speed is still a threat to water supplies. World groundwater aquifers provide approximately 23% of the freshwater used throughout the world, but the aquifers are replenished slowly by rainfall, with an average recharge rate ranging from 0.1% to 3% per year (Pimentel, 2006).

More than 99% of food comes from the land, which means that soil quality directly affects daily life of human-being. Soil is also a reservoir

of biodiversity, a carrier for nutrients and water cycling due to its driver function for chemical and biological processes. In addition, dead organic matters can be decomposed to simple forms for organisms reusing and chemical compounds harmful to humans would be absorbed or destroyed by the soil (Dominati et al., 2010). However, climate change and global warming are progressively taking place. Sea level rising causes saline water intrusion into groundwater aquifers near the coasts. Water salinization makes water harder for plants to take up or even lowers soil quality and destroys roots, leading to the loss of biodiversity, deforestation increase, desertification and soil erosion. In terms of climate regulation function, soil water affects climate patterns at short time scale, and sequesters carbon or greenhouse gases which affect air quality in the long term scale (Vereecken et al., 2010, 2016). Therefore, soil nature is also a significant aspect to be focused on.

Monitoring soil water content (SWC) is one of the practical strategies for understanding hydrological processes, weather and climate predictions, pollution assessment, etc. Near surface SWC provides valuable information for root-zone water storage and soil moisture profiles estimation (Camillo and Schmugge, 1983), and reference

^{*} Corresponding author.

^{**} Corresponding author.

E-mail addresses: kaijun.wu@student.uclouvain.be (K. Wu), sebastien.lambot@uclouvain.be (S. Lambot).

information for irrigation and fertilization as well. Ground-penetrating radar (GPR) has proven to be one of the promising methods for SWC measurements due to its high resolution and non-destructive properties. Klotzsche et al. (2018) reviewed soil moisture estimation techniques using GPR, including recent developments of instrumentation, measurement and data processing methods. Regarding the application of soil moisture characterization, the use of a GPR on a drone would significantly reduce measurement works and it would not impact soil and plants during the growing season.

Unmanned Aerial Vehicles (UAV) or Micro Aerial Vehicles, being known as drones, have proven to be powerful tools in aerial environmental and agricultural monitoring, architecture, safety and an ever increasing number of fields (Floreano and Wood, 2015). Fractional cover of green vegetation can be observed at multiple scales with drones (Riihimäki et al., 2019). It has been also applied to microwave imaging with Logarithmic-periodic dipole antennas (LPDA) by Fasano et al. (2017) and Ludeno et al. (2018). Data acquired with drones are used to map woody invasive species (Kattenborn et al., 2019). Research combining drone with GPR has been a hot spot over the past few years. Numerical models for airborne GPR have been developed to simulate the response of buried targets. Analytical solutions have been developed to describe electromagnetic wave propagation from the airplane to the medium surface (Sen et al., 2003). A Commercial Noggin Plus 500 radar system (Sensors & Software, Canada) was used on a drone for snow depth determination by Machguth et al. (2006). A 1-D tomographic approach for GPR airborne detection was proposed to characterize actual locations and sizes of underground targets (Catapano et al., 2012). The ability of drone-based GPR using Synthetic Aperture Radar (SAR) algorithm for detecting metallic or dielectric targets was demonstrated by Garcia-Fernandez et al. (2019). For being mounted on a drone, an off-ground configuration and lightweight radar system are needed. Transverse electromagnetic (TEM) horn antennas are usually considered because they are easily constructed, lightweight, directive and have a relatively large gain (Mallahzadeh and Karshenas, 2009; Ježová et al., 2017). Two circularly polarized helix antennas with a frequency range of 3.1–5.1 GHz were mounted on a drone by Garcia-Fernandez et al. (2019). A time-domain drone-GPR with separated TEM horn transmitting and receiving antennas was used for landmine detection and tested through laboratory experiments (Šipoš et al., 2017). There is a comparison between LPDA and TEM horn antennas (Burr et al., 2018a, b), and it shows that TEM horn performs well even if the weight is about three times of LPDA since the horn has more focused antenna radiation pattern and less distortion.

However, the application of drone-borne GPR for soil moisture mapping is not available yet. For this specific off-ground radar configuration, the radar equation of Lambot et al. (2004a) and Lambot and André (2014) permits to accurately model the radar signal and retrieve the medium properties through full-wave inversion, which is theoretically optimal in terms of accuracy and processing automatization.

The objective of this paper is to demonstrate the concept of soil moisture mapping with drone-based GPR and full-wave inversion. We present a new air-borne frequency-domain GPR prototype, mainly made of a handheld vector network analyzer (VNA), a microcomputer with a control application, and an ultra wideband home-made hybrid horn-dipole antenna with part of the design described by Ježová and Lambot (2019). Data processing was performed using full-wave inverse modeling with the radar electromagnetic model of Lambot et al. (2004a) and Lambot and André (2014). In this paper, inversion is performed in the time domain and focuses on the surface reflection only (Lambot et al., 2006b; Minet et al., 2012). As only two unknowns have to be retrieved for this particular configuration, namely, antenna height above the ground and soil dielectric permittivity, a look-up table (LUT) approach is used for real-time, full-wave inversion. The use of a LUT versus an optimization algorithm also leads to robustness during inversion as the objective function is fully calculated, and hence, its minimum can be found with certainty. The drone-radar-antenna system



Fig. 1. Prototype of the hybrid horn-dipole antenna mounted on the drone.

and the individual radar-antenna were characterized through global reflection and transmission functions to highlight antenna-drone interactions. Drone-GPR data acquisitions were performed in three different agricultural fields in central Belgium. The consistency of the obtained soil moisture maps was evaluated by comparing with the digital elevation models of the field as well as with orthophotography observations.

2. Drone-borne GPR

2.1. Radar and control system

The radar and its control system mainly contain (1) a lightweight vector network analyzer (Planar R60, Copper Mountain Technologies, Indianapolis, USA), (2) a transmitting and receiving (monostatic) antenna, (3) an Intel® Compute Stick with a power bank, and (4) a smartphone. The equipment introduced above is mounted on the drone as shown in Fig. 1.

The Planar R60 VNA works as the radar system unit, thereby setting up a stepped-frequency continuous-wave (SFCW) radar. With its relatively small dimensions ($130 \times 65 \times 28$ mm) and a weight of about 350 g, this USB-powered Planar R60 VNA is a 50Ω 1-port VNA capable of measuring the reflection coefficient S_{11} from 1 MHz to 6 GHz. This ultrawide bandwidth covers all traditional GPR frequencies and, therefore, permits to tune characterization depth. Its compactness readily enables direct connection to the device under test (DUT), namely, the transmitting and receiving radar antenna in this case. This eliminates losses and uncertainty associated with a coaxial cable. The VNA application connects to the R60 with a standard USB cable, creating a solution that significantly enhances ease of use compared with conventional VNA instruments. The measurement dynamic range is -105 dB with a 100 Hz IF bandwidth. The measurement speed reaches 100 μ s per frequency. The highest output power is -3 dBm (0.5 mW). The power consumption is 3.5 W. For high accuracy measurements, the VNA has to be calibrated using Open-Short-Match calibration standards. Calibration allows for correction of the errors caused by imperfections in the measurement system, namely, system directivity, source match, and tracking. The calibration is necessary to ensure repeatability of the measurements in a full-wave inversion framework.

The Intel® Compute Stick provides a platform for controlling the radar system, namely, the start and stop of measurements, and also for some presets including operating frequency range, frequency steps, and data saving directory and format. The Intel® Compute Stick dimensions are $125 \times 38 \times 12$ mm and its weight is 60 g. The operating system is Windows 10. The computer is powered by a micro-USB connector fed with 5 V (i.e., smartphone-type power bank in this case). An application

corresponding to the VNA is installed in the microcomputer, so the VNA can be remotely controlled by means of user programs written with Component Object Model (COM) technology. The COM technology is used when a user program runs together with an external measurement instrument program on the computer connected to the VNA. Presently, the measurement data is stored on the microcomputer and is subsequently post-processed on another computer. Thanks to the LUT approach, just a few minutes are required to invert several thousands of radar measurements.

A smartphone, tablet or computer is used separately by users to control the radar measurements. We developed Python and Javascript programs to remotely control the micro-computer. These programs are remotely triggered by the smartphone connected to the Intel® Compute Stick through a local Wi-Fi network launched by the microcomputer itself (external USB module). An HTTP server was set up using Node.js on the computer to provide the user interface.

2.2. Antenna design

The proposed hybrid antenna combines a tapered TEM horn (Ježová and Lambot, 2019) and a half-wave dipole covering a wide frequency range, i.e., 250–2800 MHz. The dipole was built in the continuation of the horn-part aperture to cover lower frequencies without significantly increasing the antenna dimension and weight.

An air-coupled antenna matches the feed line (with the characteristic impedance of 50 Ω) and the free space (with the intrinsic impedance of $120\pi \Omega$). The variation of impedance can be linear, exponential, Hecken, etc. The linear variation of antenna impedance $Z(z_i)$ was chosen for this prototype. The horn-part design followed the concept presented by Ježová et al. (2017) and Ježová and Lambot (2019), where the length of the horn is determined by:

$$L = 4 \times \frac{c}{f_{min}} \quad (1)$$

in which c is the speed of light in vacuum (3×10^8 m/s) and f_{min} is the lowest operating frequency. The distance between the two plates is given by:

$$d(z_i) = ae^{bz_i} \quad (2)$$

with

$$a = d_0, \quad b = \frac{1}{L} \ln \left(\frac{d_L}{d_0} \right) \quad (3)$$

where d_0 and d_L are the distance between the two plates at the feed point and the aperture, respectively. The width of each plate $w(z_i)$ is determined by:

$$w(z_i) = \frac{d(z_i)}{Z(z_i)} \eta \quad (4)$$

where η is the free space impedance.

The second part of the antenna is a dipole whose length defines the lower operating frequencies of the antenna. For this prototype, the transition between the horn part and the dipole part was made continuous but with a non-linear variation of impedance. The antenna material is 1 mm thick copper which has a great electrical conductivity, of approximately 5.96×10^7 S/m, and is relatively easy to shape. The final dimension of the antenna is $460 \times 126 \times 175$ mm. The whole GPR equipment weighs 1.5 kg.

2.3. Drone and GPS system

The drone is an X8 model made of 8 motors and 4 arms (2 motors per arm) from RCTakeOff (Overijse, Belgium), with a payload that can reach about 7 kg. The drone can support a light rain and wind speeds of up to 80 km/h.

A lightweight GPS (GlobalSat BU-353S4) is connected to the Intel®

Compute Stick for positioning of the radar data. The receiver is USB powered and outputs the GPS data in the standardized NMEA (National Marine Electronics Association) formats: GGA, GSA, GSV, and RMC, read by a Python code. Its accuracy is around 2.5 m, using the SiRF Star IV technology. The BU-353S4 is waterproof as it is a sealed unit combining the GPS module and the GPS antenna into a single circular disc. In the future, we will set up a differential GPS system for more accurate positioning.

3. Radar data processing

3.1. Radar equation

We used the radar equation of Lambot et al. (2004a) and Lambot and André (2014) to describe the radar measurements. This radar equation in particular accounts for the antennas, and inherently, interactions between the antennas and the medium, as well as three-dimensional wave propagation in multilayered media. The general form of that equation for a unique transmitting and receiving antenna, applying to both near-field and far-field conditions, is expressed in the frequency domain as follows:

$$S(\omega) = \frac{b(\omega)}{a(\omega)} = R_i(\omega) + \mathbf{T}_s(\mathbf{I}_N - \mathbf{G}^0 \mathbf{R}_s)^{-1} \mathbf{G}^0 \mathbf{T}_i \quad (5)$$

with

$$\mathbf{T}_i = [T_{i,1}(\omega) \quad T_{i,2}(\omega) \quad \cdots \quad T_{i,N}(\omega)]^T \quad (6)$$

$$\mathbf{T}_s = [T_{s,1}(\omega) \quad T_{s,2}(\omega) \quad \cdots \quad T_{s,N}(\omega)] \quad (7)$$

$$\mathbf{R}_s = \text{diag}([R_{s,1}(\omega) \quad R_{s,2}(\omega) \quad \cdots \quad R_{s,N}(\omega)]) \quad (8)$$

$$\mathbf{G} = \begin{bmatrix} G_{11}(\omega) & G_{12}(\omega) & \cdots & G_{1N}(\omega) \\ G_{21}(\omega) & G_{22}(\omega) & \cdots & G_{2N}(\omega) \\ \vdots & \vdots & & \vdots \\ G_{N1}(\omega) & G_{N2}(\omega) & \cdots & G_{NN}(\omega) \end{bmatrix} \quad (9)$$

and

$$\mathbf{G}^0 = \begin{bmatrix} G_{11}^0(\omega) & G_{12}^0(\omega) & \cdots & G_{1N}^0(\omega) \\ G_{21}^0(\omega) & G_{22}^0(\omega) & \cdots & G_{2N}^0(\omega) \\ \vdots & \vdots & & \vdots \\ G_{N1}^0(\omega) & G_{N2}^0(\omega) & \cdots & G_{NN}^0(\omega) \end{bmatrix} \quad (10)$$

where $S(\omega)$ is the radar signal measured by the VNA (S_{11} in this case) with ω being the angular frequency, $R_i(\omega)$ is the global reflection coefficient of the antenna for fields incident from the radar reference plane onto the source point, corresponding to the free-space antenna response, $T_{s,1}(\omega)$ is the global transmission coefficient for fields incident from the field point onto the radar reference plane, $T_{i,1}(\omega)$ is the global transmission coefficient for fields incident from the radar reference plane onto the source point, $R_{s,1}(\omega)$ is the global reflection coefficient for fields incident from the layered medium onto the field point, \mathbf{I}_N is the N -order identity matrix with N being the number of source and field points and superscript \top denotes transpose. The source-field points correspond to the antenna phase centers. The Green's function $G_{\cdot}(\omega)$ is defined as the scattered x -directed electric field $E_{x_{\cdot}}(\omega)$ at a field point for a unit-strength x -directed electric source $J_{x_{\cdot}}$ at a source point. The Green's function is derived using a recursive scheme to compute the global reflection coefficients of the multilayered medium in the spectral domain (Slob and Fokkema, 2002). The transformation back to the spatial domain is performed by evaluating numerically a semi-infinite integral (e.g., see Lambot et al. (2007)).

In far-field conditions (Lambot et al., 2004b; Tran et al., 2013), a single source and field point ($N = 1$) is sufficient to describe the radar signal. In that case, Eq. (5) reduces to:

$$S(\omega) = R_i(\omega) + \frac{T_{s,1}(\omega)G_{xx}(\omega)T_{i,1}(\omega)}{1 - G_{xx}(\omega)R_{s,1}(\omega)} \quad (11)$$

where $R_i(\omega)$ can be measured directly by the VNA in free space in which $G_{xx}(\omega) = 0$, so $S_{11}(\omega) = R_i(\omega)$. We define $T(\omega) = T_{s,1}(\omega)T_{i,1}(\omega)$ as the transmitting-receiving response function. $R_i(\omega)$, $T(\omega)$ and $R_{s,1}(\omega)$ can be obtained by solving a system of linear equations as described by Lambot et al. (2006a). Once the antenna characteristic functions are known, the measured Green's function $G_{xx}(\omega)$ can be calculated from Eq. (11) as:

$$G_{xx}(\omega) = \frac{S(\omega) - R_i(\omega)}{T(\omega) + S(\omega)R_{s,1}(\omega) - R_i(\omega)R_{s,1}(\omega)} \quad (12)$$

3.2. Drone-antenna calibration

In order to apply this model, the calibration of the antenna, i.e., determining its global reflection and transmission coefficients, should be done. We set the frequency range to 200–3200 MHz with a frequency step of 10 MHz for the calibration. Calibration was carried out using measurements with the antenna situated at 6 different distances (50–70 cm interval with a step of 4 cm) from a large copper sheet (3 m × 3 m). In order to evaluate the effect of the drone on the radar measurements, we performed the calibration of the antenna with and without the drone. The results are presented in Fig. 2.

Qualitatively, there is not a large difference between the two calibrations. An antenna in free space can be considered to perform well when the magnitude of its free space response, so called return loss, R_i , is less than 0.5, corresponding to a voltage standing wave ratio (VSWR) less than 3. We observe in Fig. 2a that the operating frequency ranges for the two configurations are almost the same, namely, 245–2883 MHz for the drone-antenna and 246–2860 MHz for the antenna alone, respectively. Nevertheless, quantitatively, in a full-wave inversion framework, these differences are significant. The global transmission functions of the antenna for the two configurations, denoting gain, present both a similar shape, but with more significant differences in the lower frequency range. Indeed, the lower frequencies are expected to be more affected by the conductive structures of the drone, mainly made of conductive carbon and wires. The phase of T for both configurations are generally linear, which indicates that the antenna is not very dispersive. Dispersivity of the antenna is however not an issue in a full-wave modeling framework as it is part of the model. The presence of the drone also affects the return loss for the backscattered field from the medium, namely, R_s , especially in the lower frequency range. These results indicate that for proper signal modeling, it is necessary to calibrate the antenna mounted on the drone to include antenna-drone interactions (multiple reflections).

3.3. Full-wave inversion

The least-squares formulation is used to define the inverse problem and the objective function to be minimized is accordingly defined as:

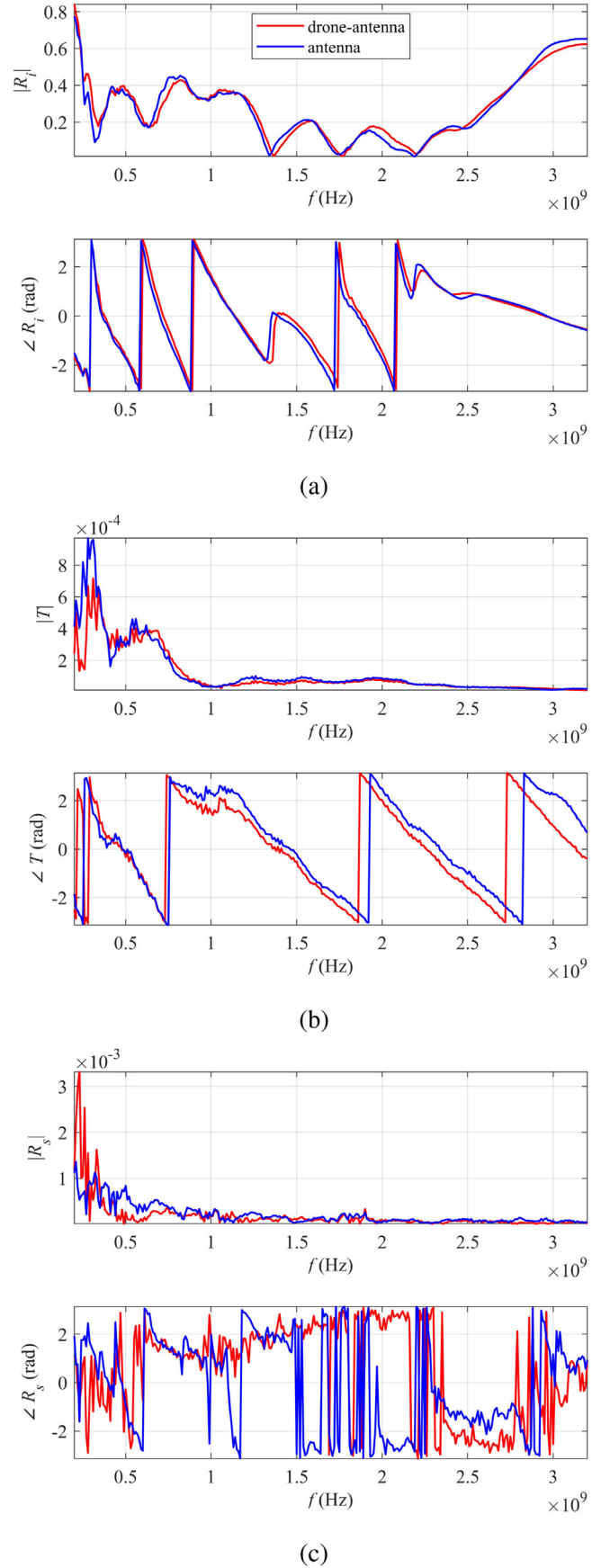
$$\phi(\mathbf{b}) = (\mathbf{g}_{xx}^*(t) - \mathbf{g}_{xx}^{\dagger}(\mathbf{b}, t))^T (\mathbf{g}_{xx}^*(t) - \mathbf{g}_{xx}^{\dagger}(\mathbf{b}, t)) \quad (13)$$

where $\mathbf{g}_{xx}^*(t)$ and $\mathbf{g}_{xx}^{\dagger}(\mathbf{b}, t)$ are the measured and modeled Green's functions in the time domain.

The measured $\mathbf{g}_{xx}^*(t)$ can be obtained from $G_{xx}(\omega)$ using the inverse Fourier transform as:

$$\mathbf{g}_{xx}^*(t) = F^{-1}\{\mathbf{G}_{xx}(\omega)\} = \frac{1}{2\pi} \int_{-\infty}^{\infty} e^{i\omega t} \mathbf{G}_{xx}(\omega) d\omega \quad (14)$$

where $\mathbf{b} = [\mathbf{h}_0, \varepsilon_r]$ is the parameter matrix of the inverse problem with \mathbf{h}_0 being the vector of the distance between the antenna phase center and the soil surface and ε_r being the vector of the relative dielectric permittivity. Hence, changes in flight altitude do not affect the results, except regarding the signal-to-noise ratio, which decreases with the height increasing.



(caption on next page)

Fig. 2. Magnitude and phase of the antenna characteristic functions for individual antenna (blue curves) and the drone-antenna systems (red curves). (a) The return loss R_r , (b) transmitting-receiving response function T and (c) the feedback loss R_r . (For interpretation of the references to color in this figure legend, the reader is referred to the Web version of this article.)

The objective function is calculated in the full parameter space and optimized by comparing the measured Green's function with the pre-computed once stored in a look-up table (LUT). We fixed

$$\mathbf{h}_0 = [0.500 \ 0.505 \ 0.510 \ \dots \ 5.995 \ 6.000]^T$$

$$\varepsilon_r = [2.0 \ 2.5 \ 3.0 \ \dots \ 29.5 \ 30.0]^T$$

resulting in 1101×57 calculations in total (i.e., 62757 values). The LUT is suitable for fast and robust inversion when only two parameters have to be estimated because the LUT has only to be calculated once (Rajaram et al., 2008; Gastellu-Etchegorry et al., 2003; Kim et al., 2011).

In this study, we used the petrophysical relation of Topp et al. (1980) to estimate the volumetric soil moisture θ based on the relative dielectric permittivity ε_r :

$$\theta = -5.3 \times 10^{-2} + 2.92 \times 10^{-2} \varepsilon_r - 5.5 \times 10^{-4} \varepsilon_r^2 + 4.3 \times 10^{-6} \varepsilon_r^3 \quad (15)$$

4. Soil moisture maps

The measurements were performed over three different bare agricultural fields with different topographical conditions in the region of Gembloux, Walloon region, Belgium (see Fig. 3): field F1 in Cinq Etoiles (a gentle slope with an area of 1.13 ha, 1196 radar measurements), field F2 in Vieusart (a shallow sunken of 0.69 ha, 1238 radar measurements), field F3 in Saint-Denis (landform of 1.40 ha with a main thalweg, 2437 radar measurements), respectively. The distance between the radar measurement points within each track line is around 1 m, and the distance between track lines is about 4 m, representing about 1500 points per ha on average. All of these test fields are located within the central Belgian loess belt, with mainly sandy-loam and silt-loam soils. The loess belt occupies a low plateau extending from the west to the east across the central part of Belgium (Van den Haute et al., 2003). The spatial distribution of soil erosion and sediment deposition within the catchments strongly depend on slope gradient and position within the catchment (Rommens et al., 2005). Walloon covers an area of 1,680,000 ha in southern Belgium, approximately 45% of which is occupied by loess-derived soils, mainly loess-derived Luvisols (silt loam

texture). Agricultural runoff floods dominate in the silt-loam and sandy-loam agricultural regions, so the soils are susceptible to surface sealing and erosion when cropped (Biélders et al., 2003).

In the encountered field conditions, the effects of soil roughness become significant above 700 MHz according to Rayleigh's criterion (Lambot et al., 2006a). Yet, soil roughness was not accounted for in this version of the electromagnetic model. In addition, for a given flying height, the higher the frequencies are, the smaller the signal-to-noise-ratio is. For these reasons, we set 700 MHz as maximum frequency for the radar data processing. Between 400 MHz and 500 MHz, we observed a poor radar data quality. The reason remains to be elucidated, but it may arise from less antenna directivity in that frequency range and/or drone interferences. Yet, the VSWR of the antenna remains good in that range. In order to use a continuous frequency range, we therefore set it as 500–700 MHz for processing the radar data, which provides information on the top 10–20 cm of soil when focusing on the surface reflection. The frequency step was fixed to 10 MHz. Flights were performed manually. The flying altitude ranged between about 1 m and 5 m. In this study, the flying altitude was limited to ensure always a good signal-to-noise ratio. In addition, the far-field assumption in the electromagnetic model was always respected (Lambot and André, 2014; Tran et al., 2013). About 4–5 measurements were acquired per second. The fields were mapped within less than 15 min.

4.1. Test site in Cinq Etoiles

For the site in Cinq Etoiles (F1), the radar-derived soil moisture at each measurement point is presented in Fig. 4a. Firstly, the observed soil moisture values fall well within the possible values of soil moisture. In that respect, it is worth noting that the full-wave inversion is purely physical, which means that there is no calibration to relate soil moisture to the radar signal. Inversion outliers were removed. Outliers represent the worse model fits, and were defined as the points whose minima of the objective functions are larger than the average value of the objective function minima of all points plus 2 times the standard deviation. However, we could also observe that the distribution of the measurement points over the field is not perfectly uniform due to the manual mode flight. The observed soil moisture semivariogram is shown in Fig. 4b. The spatial correlation of soil moisture reaches about 100 m. A nugget effect is also observed, which corresponds to about half of the total field variability. This nugget effect either results from a significant micro-variability of soil moisture or measurement errors. The later are seemingly due to the limited stability of the drone during the flight, changing the incidence angle when accelerating or decelerating. The orientation of the antenna with respect to the soil surface is presently not included in the antenna calibration. Changes in the drone-antenna interactions are also expected to occur (e.g., rotation of the conductive carbon propellers).

The corresponding, continuous soil moisture map, depicted in Fig. 5a, was obtained by the kriging interpolation method. The digital elevation model of the field is presented in Fig. 5b. This elevation model was obtained from aerial drone photographs using photogrammetry. Photogrammetry processing was performed using the Agisoft MetaShape software. We used the DJI Phantom 4 Pro with a flying height of 90 m for the data acquisition. The resolution of the surface model is about 5 cm.

The test plot F1 is situated in a small catchment, and the whole test site presents a gentle slope with a maximum altitude difference of about 5 m. The height goes down from the south to the north (see Fig. 5b). The soil moisture map also appears to be very consistent with the topography of the field. The top of the hill and the slope are the driest parts of the field while the bottom is the wettest. Regarding the changes of incidence angle due to the soil topography, we note that to top of the field and the bottom of the field, both being relatively flat, present very different soil moisture. The top of the field and the slope present similar soil moisture while the slope is different. This indicates that the effect of

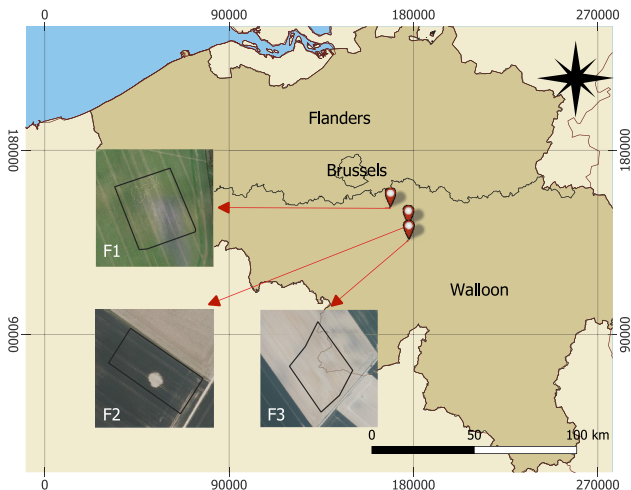
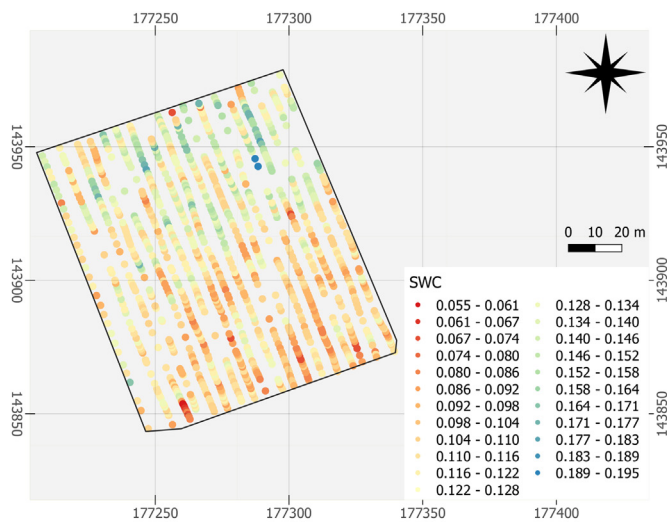
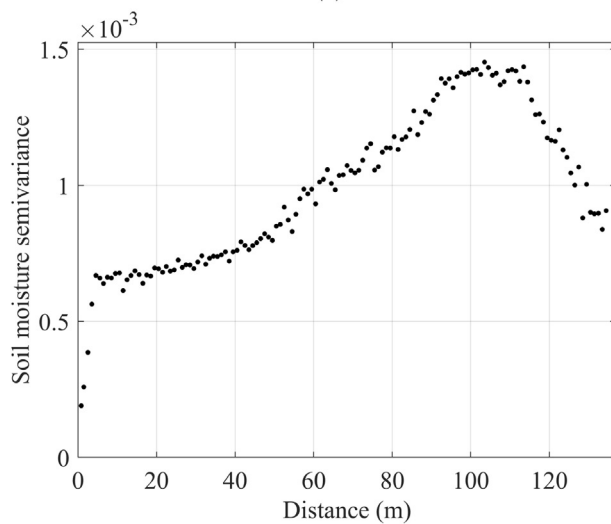


Fig. 3. Locations of the three agricultural fields (F1–F3) in the loess belt region in Belgium. Coordinates are in Belgian Lambert 72 (m).



(a)



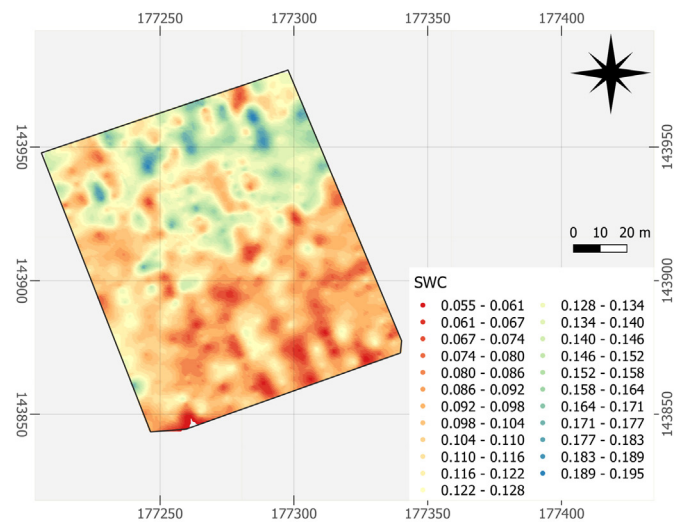
(b)

Fig. 4. (a) Volumetric soil water content measurement points in Cinq Etoiles (F1). Coordinates are in Belgian Lambert 72 (m). (b) Corresponding semivariogram for soil moisture of F1.

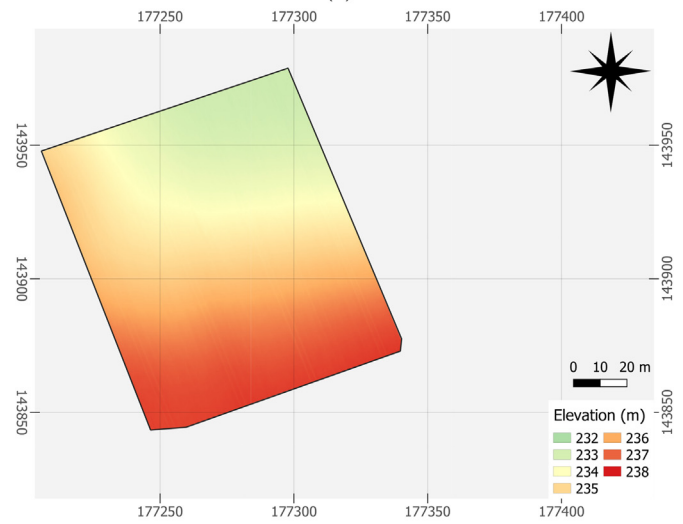
the slope on the radar measurements was much smaller than the effect of the soil moisture variability. Neglecting the incidence angle in these conditions seems therefore a good approximation. This results from the nearly isotropic gain of the antenna in that frequency range for small angles.

4.2. Test site in Vieuart

Fig. 6 shows the soil moisture map and the elevation map of the site in Vieuart (F2), near Louvain-la-Neuve (Belgium). Compared to the radar acquisitions in the field F1, the radar measurements in F2 were acquired with a density approximately two times larger. A picture taken during the measurements is also presented to show a comparatively wet area where ponding regularly appears in this field (Fig. 7). This area contains a gentle sunken in one of the lowest parts of the field (see Fig. 6b), in the center of which some ponding can be seen. As we can see in Fig. 7, this ponding area prevents vegetation to grow. This wet area is well visible on the soil moisture map (see Fig. 6a). The estimated moisture is however not the saturated one as the radar measurements were not specifically acquired exactly on top of the ponding area. The driest part of the soil moisture map is in the east, which also



(a)



(b)

Fig. 5. Agricultural field in Cinq Etoiles (F1), Belgium. (a) Soil moisture map and (b) digital elevation map. Coordinates are in Belgian Lambert 72 (m).

corresponds to the highest parts and slopes of the field.

4.3. Test site in Saint-Denis

The results for the test site in Saint-Denis, situated in the south of Gembloux (Belgium), are presented in Fig. 8. During the radar measurements, the soil was fully bared, which permitted to observe its color variations (see aerial orthophotography in Fig. 8c). In particular, this orthophotography shows different colors related to soil surface texture distributions, with the lighter areas corresponding to silt accumulated through erosion and the darker areas containing more clay and organic matter. As shown in the elevation model (Fig. 8b), this terrain is relatively complex compared with the fields F1 and F2, including flat areas, slight slopes and a gentle thalweg. In the soil moisture map, a wet area extends from the south of the field to its center, and there is a drier area in the south-western part of the field. There is a good correspondence between the soil moisture map and the elevation map. In addition, the soil moisture map also has a good correlation with the soil orthophotography. Indeed, the soil color is related to its texture, which defines the soil hydraulic properties controlling soil moisture dynamics. The darker area in the northern part of the field (see Fig. 8c) corresponds to the dry area in the north (see Fig. 8a). In conclusion, both the elevation

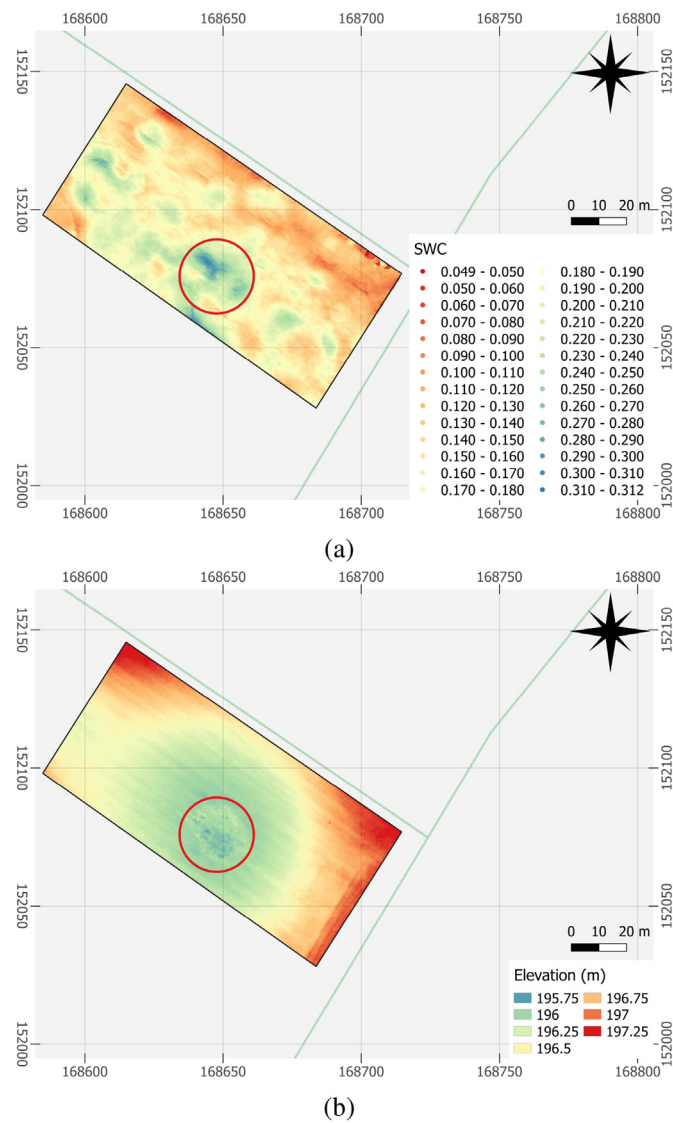


Fig. 6. Agricultural field in Vieuxart (F2), Belgium. (a) Soil moisture map, (b) digital elevation model. Coordinates are in Belgian Lambert 72 (m).



Fig. 7. Picture taken during the measurements showing a particularly wet area (see corresponding surrounded area in Fig. 6).

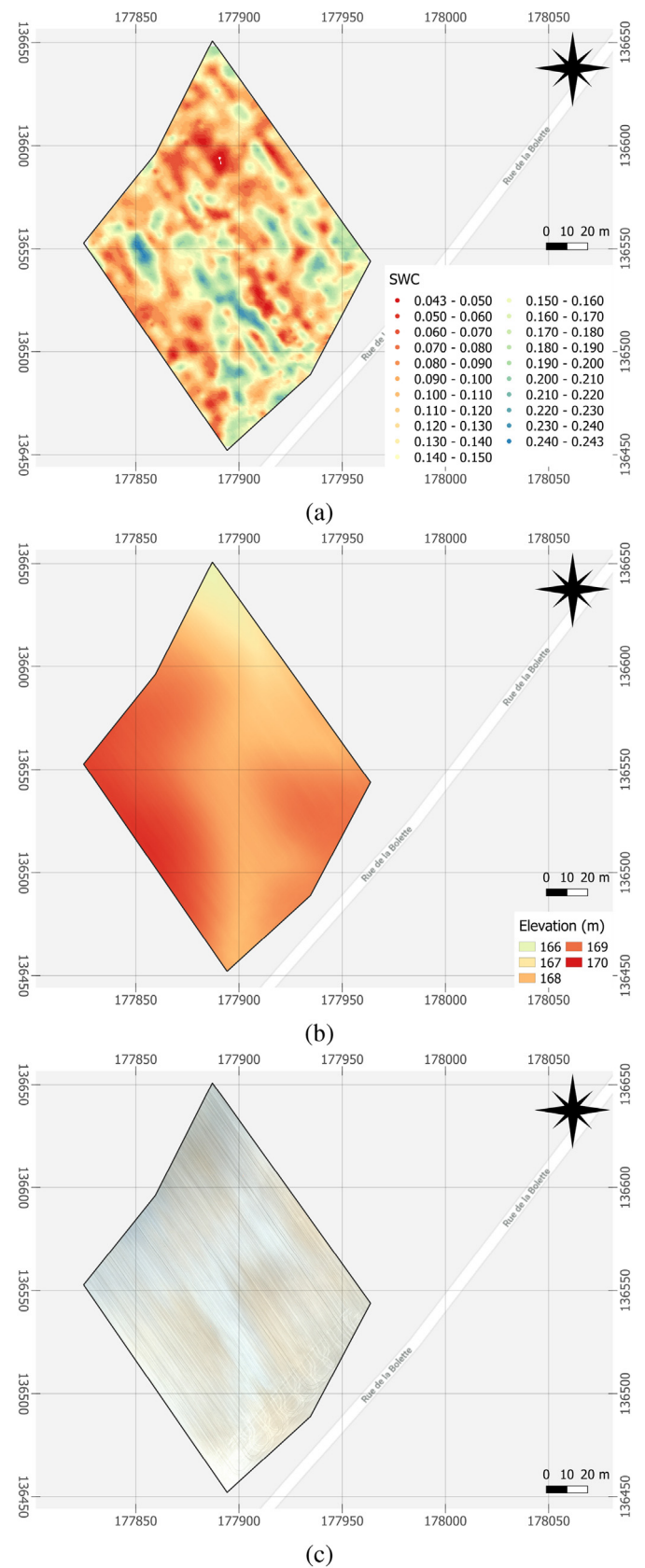


Fig. 8. Agricultural field in Saint-Denis (F3), Belgium. (a) Soil moisture map, (b) digital elevation model and (c) soil orthophotography. Coordinates are in Belgian Lambert 72 (m).

model and soil orthophotography demonstrate the consistence of the soil moisture results in the field in Saint-Denis.

5. Conclusions and perspectives

We presented a new lightweight, drone-borne frequency-domain GPR for soil moisture mapping. The system is made of a mini vector network analyzer (VNA), an ultra wideband hybrid horn-dipole antenna and controlling devices. The VNA is controlled by an Intel® Computer Stick, itself remotely controlled by a graphical user interface using a local HTTP server, local Wi-Fi hotspot and smartphone. Full-wave inversion focused on the surface reflection in the time domain was applied to retrieve soil permittivity and correlated moisture. The characterization of the antenna global reflection and transmission functions indicated that the drone affects the antenna radiation properties, and hence, should be part of the calibration for proper inversion. A look-up table (LUT) approach was used to solve the inverse problem, which permits real-time inversion on a single processor as well as robustness (the global minimum of the objective function is always found). We presented high-resolution soil moisture maps obtained in three different agricultural fields in Belgium. These fields were chosen as their soil moisture is mainly controlled by topography, which can be readily characterized using aerial drone photogrammetry.

The three soil moisture maps presented show good agreements with the corresponding elevation maps. This constitutes a first step in the validation of the proposed technique. The drone-based GPR prototype has demonstrated that the developed tools are operational and provide consistent results in terms of spatial patterns as well as in terms of absolute soil moisture values. However, the radar measurements are still subject to errors, which may come from drone-antenna interactions as well as variations in the incidence angle due to flight instabilities and soil slope. Changes in the incidence angle is presently not taken into account in the antenna calibration.

Our future research will focus on (1) the calibration of the full-wave antenna model with taking account to incidence angle and the inversion with considering the soil roughness, (2) threshold of objective function formulation based on acceptable confidence intervals on the estimates, (3) the improvement of the antenna design for better gain and directivity to improve the signal-to-noise ratio, and (4), when this will be achieved, the validation using comparisons with extensive ground-truths to better understand the observed variability in the soil moisture map. Finally, a drone flying controlling system will be applied to achieve automatic flying for better stability and more uniform sampling.

Acknowledgments

This research was funded by the Politique Scientifique Fédérale (BELSPO, Belgium) in the frame of the Research Programme for Earth Observation STEREO III, RAPAS project (contract SR/00/238) and the Fonds de la Recherche Scientifique (FNRS, Belgium). This research was also carried out within the framework of EU COST Action TU 1208 “Civil Engineering Applications of Ground-Penetrating Radar”.

References

- Bielders, C.L., Ramelot, C., Persoons, E., 2003. Farmer perception of runoff and erosion and extent of flooding in the silt-loam belt of the Belgian Walloon region. *Environ. Sci. Policy* 6, 85–93. [https://doi.org/10.1016/S1462-9011\(02\)00117-X](https://doi.org/10.1016/S1462-9011(02)00117-X).
- Burr, R., Schartel, M., Mayer, W., Walter, T., Waldschmidt, C., 2018a. Lightweight broadband antennas for uav based gpr sensors. In: 2018 15th European Radar Conference, pp. 245–248. <https://doi.org/10.23919/EuRAD.2018.8546552>. EuRAD 2018.
- Burr, R., Schartel, M., Schmidt, P., Mayer, W., Walter, T., Waldschmidt, C., 2018b. Design and implementation of a fmcw gpr for uav-based mine detection. In: 2018 IEEE MTT-S International Conference on Microwaves for Intelligent Mobility, <https://doi.org/10.1109/ICMIM.2018.8443526>. ICMIM 2018.
- Camillo, P., Schumge, T.J., 1983. Estimating soil moisture storage in the root zone from surface measurements. *Soil Sci.* 135, 245–264. <https://doi.org/10.1097/00010694-198304000-00006>.
- Catapano, I., Crocco, L., Krellmann, Y., Triltsch, G., Soldovieri, F., 2012. A tomographic approach for helicopter-borne ground penetrating radar imaging. *IEEE Geosci. Remote Sens. Lett.* 9, 378–382. <https://doi.org/10.1109/LGRS.2011.2169390>.
- Dominati, E., Patterson, M., Mackay, A., 2010. A framework for classifying and quantifying the natural capital and ecosystem services of soils. *Ecol. Econ.* 69, 1858–1868. <https://doi.org/10.1016/j.ecolecon.2010.05.002>.
- Fasano, G., Renga, A., Vetrella, A.R., Ludeno, G., Catapano, I., Soldovieri, F., 2017. Proof of Concept of Micro-uav-based Radar Imaging. Institute of Electrical and Electronics Engineers Inc., pp. 1316–1323. <https://doi.org/10.1109/ICUAS.2017.7991432>.
- Floreano, D., Wood, R.J., 2015. Science, technology and the future of small autonomous drones. *Nature* 521, 460–466. <https://doi.org/10.1038/nature14542>.
- Garcia-Fernandez, M., Alvarez-Lopez, Y., Heras, F.L., Gonzalez-Valdes, B., Rodriguez-Vaqueiro, Y., Pino, A., Arboleya-Arboleya, A., 2019. Gpr system onboard a uav for non-invasive detection of buried objects. In: 2018 IEEE Antennas and Propagation Society International Symposium and USNC/URSI National Radio Science Meeting, APSURSI 2018 - Proceedings, pp. 1967–1968. <https://doi.org/10.1109/APUSNCURSINRSM.2018.8608907>.
- Gastellu-Etcheberry, J.P., Gascon, F., Estève, P., 2003. An interpolation procedure for generalizing a look-up table inversion method. *Remote Sens. Environ.* 87, 55–71. [https://doi.org/10.1016/S0034-4257\(03\)00146-9](https://doi.org/10.1016/S0034-4257(03)00146-9).
- Ježová, J., Lambot, S., 2019. A dielectric horn antenna and lightweight radar system for material inspection. *J. Appl. Geophys.* 103822. <https://doi.org/10.1016/j.jappgeo.2019.103822>.
- Ježová, J., Lambot, S., Fedeli, A., Randazzo, A., 2017. Ground-penetrating radar for tree trunk investigation. In: 2017 9th International Workshop on Advanced Ground Penetrating Radar, IWAGPR 2017 - Proceedings, <https://doi.org/10.1109/IWAGPR.2017.7996079>.
- Kattenborn, T., Lopatin, J., Förster, M., Braun, A.C., Fassnacht, F.E., 2019. Uav data as alternative to field sampling to map woody invasive species based on combined sentinel-1 and sentinel-2 data. *Remote Sens. Environ.* 227, 61–73. <https://doi.org/10.1016/j.rse.2019.03.025>. export Date: 24 April 2019.
- Kim, S.B., Huang, S., Tsang, L., Johnson, J., Njoku, E., 2011. Soil moisture retrieval over low-vegetation surfaces using time-series radar observations and a lookup table representation of forward scattering. In: International Geoscience and Remote Sensing Symposium (IGARSS), pp. 146–149. <https://doi.org/10.1109/IGARSS.2011.6048919>.
- Klotzsche, A., Jonard, F., Looms, M.C., van der Kruk, J., Huisman, J.A., 2018. Measuring soil water content with ground penetrating radar: a decade of progress. *Vadose Zone J.* 17. <https://doi.org/10.2136/vzj2018.03.0052>.
- Lambot, S., André, F., 2014. Full-wave modeling of near-field radar data for planar layered media reconstruction. *IEEE Trans. Geosci. Remote Sens.* 52, 2295–2303. <https://doi.org/10.1109/TGRS.2013.2259243>.
- Lambot, S., Slob, E.C., Van Bosch, I.D., Stockbroeckx, B., Vanclooster, M., 2004a. Modeling of ground-penetrating radar for accurate characterization of subsurface electric properties. *IEEE Trans. Geosci. Remote Sens.* 42, 2555–2568. <https://doi.org/10.1109/TGRS.2004.834800>.
- Lambot, S., Rhebergen, J., van den Bosch, I., Slob, E.C., Vanclooster, M., 2004b. Measuring the soil water content profile of a sandy soil with an off-ground monostatic ground penetrating radar. *Vadose Zone J.* 3, 1063–1071. <https://doi.org/10.2113/3.4.1063>.
- Lambot, S., Antoine, M., Vanclooster, M., Slob, E.C., 2006a. Effect of soil roughness on the inversion of off-ground monostatic gpr signal for noninvasive quantification of soil properties. *Water Resour. Res.* 42. <https://doi.org/10.1029/2005WR004416>.
- Lambot, S., Weihermüller, L., Huisman, J.A., Vereecken, H., Vanclooster, M., Slob, E.C., 2006b. Analysis of air-launched ground-penetrating radar techniques to measure the soil surface water content. *Water Resour. Res.* 42. <https://doi.org/10.1029/2006WR005097>.
- Lambot, S., Slob, E.C., Vereecken, H., 2007. Fast evaluation of zero-offset green's function for layered media with application to ground-penetrating radar. *Geophys. Res. Lett.* 34. <https://doi.org/10.1029/2007GL031459>.
- Ludeno, G., Catapano, I., Renga, A., Vetrella, A.R., Fasano, G., Soldovieri, F., 2018. Assessment of a micro-uav system for microwave tomography radar imaging. *Remote Sens. Environ.* 212, 90–102. <https://doi.org/10.1016/j.rse.2018.04.040>.
- Machguth, H., Eisen, O., Paul, F., Hoelzle, M., 2006. Strong spatial variability of snow accumulation observed with helicopter-borne gpr on two adjacent alpine glaciers. *Geophys. Res. Lett.* 33. <https://doi.org/10.1029/2006GL026576>.
- Mallahzadeh, A.R., Karshenas, F., 2009. Modified tem horn antenna for broadband applications. *Prog. Electromagn. Res.* 90, 105–119. <https://doi.org/10.2528/PIER08123106>.
- Minet, J., Bogaert, P., Vanclooster, M., Lambot, S., 2012. Validation of ground penetrating radar full-waveform inversion for field scale soil moisture mapping. *J. Hydrol.* 424–425, 112–123. <https://doi.org/10.1016/j.jhydrol.2011.12.034>.
- Oki, T., Kanae, S., 2006. Global hydrological cycles and world water resources. *Science* 313, 1068–1072. <https://doi.org/10.1126/science.1128845>.
- Pimentel, D., 2006. Soil erosion: a food and environmental threat. *Environ. Dev. Sustain.* 8, 119–137. <https://doi.org/10.1007/s10668-005-1262-8>.
- Pimentel, D., Berger, B., Filiberto, D., Newton, M., Wolfe, B., Karabinakis, E., Clark, S., Poon, E., Abbott, E., Nandagopal, S., 2004. Water resources: agricultural and environmental issues. *Bioscience* 54, 909–918. [https://doi.org/10.1641/0006-3568\(2004\)054\[0909:WRAAEI\]2.0.CO;2](https://doi.org/10.1641/0006-3568(2004)054[0909:WRAAEI]2.0.CO;2).
- Rajaram, N., Nguyen, T.H., Tunnell, J.W., 2008. Lookup table-based inverse model for determining optical properties of turbid media. *J. Biomed. Opt.* 13. <https://doi.org/10.1117/1.2981797>.
- Riihimäki, H., Luoto, M., Heiskanen, J., 2019. Estimating fractional cover of tundra

- vegetation at multiple scales using unmanned aerial systems and optical satellite data. *Remote Sens. Environ.* 224, 119–132. <https://doi.org/10.1016/j.rse.2019.01.030>. export Date: 24 April 2019.
- Rommens, T., Verstraeten, G., Poesen, J., Govers, G., Van Rompaey, A., Peeters, I., Lang, A., 2005. Soil Erosion and Sediment Deposition in the Belgian Loess Belt during the Holocene: Establishing a Sediment Budget for a Small Agricultural Catchment, vol. 15 <https://doi.org/10.1191/0959683605hl876ra>.
- Sen, M.K., Stoffa, P.L., Seifoullaev, R.K., Fokkema, J.T., 2003. Numerical and Field Investigations of GPR: Toward an Airborne GPR. *Subsurf. Sens. Technol. Appl.* 4 (1), 41–60. <https://doi.org/10.1023/A:1023011413969>.
- Šipoš, D., Planinšič, P., Gleich, D., 2017. On drone ground penetrating radar for landmine detection. In: 2017 1st International Conference on Landmine: Detection, Clearance and Legislations, pp. 7–10. <https://doi.org/10.1109/LDCL.2017.7976931>. LDCL 2017.
- Slob, E., Fokkema, J., 2002. Coupling effects of two electric dipoles on an interface. *Radio Sci.* 37 <https://doi.org/10.1029/2001rs002529>. (slob, E Fokkema, J).
- Topp, G.C., Davis, J.L., Annan, A.P., 1980. Electromagnetic determination of soil water content: measurements in coaxial transmission lines. *Water Resour. Res.* 16, 574–582. <https://doi.org/10.1029/WR016i003p00574>.
- Tran, A.P., Andre, F., Craeye, C., Lambot, S., 2013. Near-field or far-field full-wave ground penetrating radar modeling as a function of the antenna height above a planar layered medium. *Prog. Electromagn. Res.-Pier* 141, 415–430. <https://doi.org/10.2528/pier13053106>.
- Van den Haute, P., Frechen, M., Buylaert, J.P., Vandenberghe, D., De Corte, F., 2003. The last interglacial palaeosol in the belgian loess belt: Tl age record. *Quat. Sci. Rev.* 22, 985–990. [https://doi.org/10.1016/S0277-3791\(03\)00023-4](https://doi.org/10.1016/S0277-3791(03)00023-4).
- Vereecken, H., Huisman, J.A., Bogen, H., Vanderborght, J., Vrugt, J.A., Hopmans, J.W., 2010. On the value of soil moisture measurements in vadose zone hydrology: a review. *Water Resour. Res.* 46. <https://doi.org/10.1029/2008WR006829>.
- Vereecken, H., Aitkenhead, M., Allison, S., Assouline, S., Baveye, P., Berli, M., Brüggemann, N., Finke, P., Flury, M., Gaiser, T., Govers, G., Schnepf, A., Ghezzehei, T., Hallett, P., Hendricks Franssen, H., Heppell, J., Horn, R., Huisman, J., Jacques, D., Jonard, F., Kollet, S., Lafolie, F., Hopmans, J., Lamorski, K., Leitner, D., McBratney, A., Minasny, B., Montzka, C., Nowak, W., Pachepsky, Y., Padarian, J., Romano, N., Roth, K., Javaux, M., Rothfuss, Y., Rowe, E., Schwen, A., Šimůnek, J., Tiktak, A., Van Dam, J., van der Zee, S., Vogel, H., Vrugt, J., Wöhling, T., Or, D., Young, I., Roose, T., Vanderborght, J., Young, M., Amelung, W., 2016. Modeling soil processes: review, key challenges, and new perspectives. *Vadose Zone J.* 15. <https://doi.org/10.2136/vzj2015.09.0131>.